

Interstellar Gas and a Dark Disk

Eric David Kramer and Lisa Randall

Department of Physics, Harvard University, Cambridge, MA, 02138

ABSTRACT

We introduce a potentially powerful method for constraining or discovering a thin dark matter disk in the Milky Way. The method relies on the relationship between the midplane densities and scale heights of interstellar gas being determined by the gravitational potential, which is sensitive to the presence of a dark disk. We show how to use the interstellar gas parameters to set a bound on a dark disk and discuss the constraints suggested by the current data. However, current measurements for these parameters are discordant, with the uncertainty in the constraint being dominated by the molecular hydrogen midplane density measurement, as well as by the atomic hydrogen velocity dispersion measurement. Magnetic fields and cosmic ray pressure, which are expected to play a role, are uncertain as well. The current models and data are inadequate to determine the disk's existence, but, taken at face value, may favor its existence depending on the gas parameters used.

1. Introduction

Fan, Katz, Randall, and Reece in 2013 proposed the existence of thin disks of dark matter in spiral galaxies including the Milky Way, in a model termed Double Disk Dark Matter (DDDM). In this model, a small fraction of the dark matter is interacting and dissipative, so that this sector of dark matter would cool and form a thin disk. More recently Randall & Reece (2014) showed that a dark matter disk of surface density $\sim 10 M_{\odot}\text{pc}^{-2}$ and scale height ~ 10 pc could possibly explain the periodicity of comet impacts on earth. It is of interest to know what values of dark disk surface density and scale height are allowed by the current data, and whether these particular values are allowed.

Since the original studies by Oort (1932, 1960), the question of disk dark matter has been a subject of controversy. Over the years, several authors have suggested a dark disk to explain various phenomena. Kalberla et al. (2007) proposed a thick dark disk as a way to explain the flaring of the interstellar gas layer. It has also been argued that a thick dark disk is formed naturally in a Λ CDM cosmology as a consequence of satellite mergers (Read et al. 2008). Besides these, there are also models arguing for a thin dark disk. Fan et al. (2013) put forward a model for dark matter where a small fraction of the total dark matter could be self-interacting and dissipative, necessarily forming a thin dark disk. In Kramer & Randall (2016) we investigated the constraints on such a disk from

stellar kinematics. In this paper we investigate the constraint imposed by demanding consistency between measurements of midplane densities and surface densities interstellar gas.

We assume a Bahcall-type model for the vertical distributions of stars and gas (Bahcall 1984a,b,c) as in Kramer & Randall (2016), with various visible mass components, as well as a dark disk. We investigate the visible components in detail given more recent measurements of both the surface and midplane densities. A dark disk affects the relationship between the two as argued in Kramer & Randall and as we review below. Although current measurements are insufficiently reliable to place strong constraints on or identify a disk, we expect this method will be useful in the future when better measurements are achieved.

2. Poisson-Jeans Theory

As explained in detail in Kramer & Randall (2016), for an axisymmetric self-gravitating system, the vertical Jeans equation near the $z = 0$ plane reads

$$\frac{\partial}{\partial z}(\rho_i \sigma_i^2) + \rho_i \frac{\partial \Phi}{\partial z} = 0. \quad (1)$$

For an isothermal population ($\sigma_i(z) = \text{constant}$), the solution reduces to

$$\rho_i(z) = \rho_i(0) e^{-\Phi(R,z)/\sigma_i^2}. \quad (2)$$

Combining this with the Poisson equation gives the Poisson-Jeans equation for the potential Φ

$$\frac{\partial^2 \Phi}{\partial z^2} = 4\pi G \sum_i \rho_i(0) e^{-\Phi/\sigma_i^2}, \quad (3)$$

which can also be cast in integral form (assuming z -reflection symmetry)

$$\frac{\rho_i(z)}{\rho_i(0)} = \exp\left(-\frac{4\pi G}{\sigma_i^2} \sum_k \int_0^z dz' \int_0^{z'} dz'' \rho(z'')\right). \quad (4)$$

This is the form used in our Poisson-Jeans solver.

2.1. A toy model

In Kramer & Randall (2016), we showed that the exact solution to the Poisson-Jeans equation for a thick component (in this case, the interstellar gas which is thick compared to the dark disk) with midplane density ρ_0 and vertical dispersion σ interacting with an infinitely thin (delta-function profile) dark disk was

$$\rho(z) = \rho_0(1 + Q^2) \operatorname{sech}^2\left(\frac{\sqrt{1 + Q^2}}{2h}(|z| + z_0)\right) \quad (5)$$

where

$$Q \equiv \Sigma_D / 4\rho_0 h, \quad (6)$$

$$h \equiv \frac{\sigma}{\sqrt{8\pi G \rho_0}}, \quad (7)$$

and

$$z_0 \equiv \frac{2h}{\sqrt{1+Q^2}} \operatorname{arctanh} \left(\frac{Q}{\sqrt{1+Q^2}} \right). \quad (8)$$

Thus, the effect of the dark disk is to ‘pinch’ the density distribution of the other components, as we can see in Figure 1. Thus, although the scale height of the gas disk is proportional to its velocity dispersion according to Equation 7, a dark disk will reduce the gas disk’s thickness relative to this value, and for a fixed midplane density $\rho_i(0)$, it implies that their surface densities Σ_i are less than what it would be without the dark disk or any other mass component. In this approximation, the gas distribution will have a cusp at the origin, but in general, the dark disk will have a finite thickness and the solution will be smooth near $z = 0$.

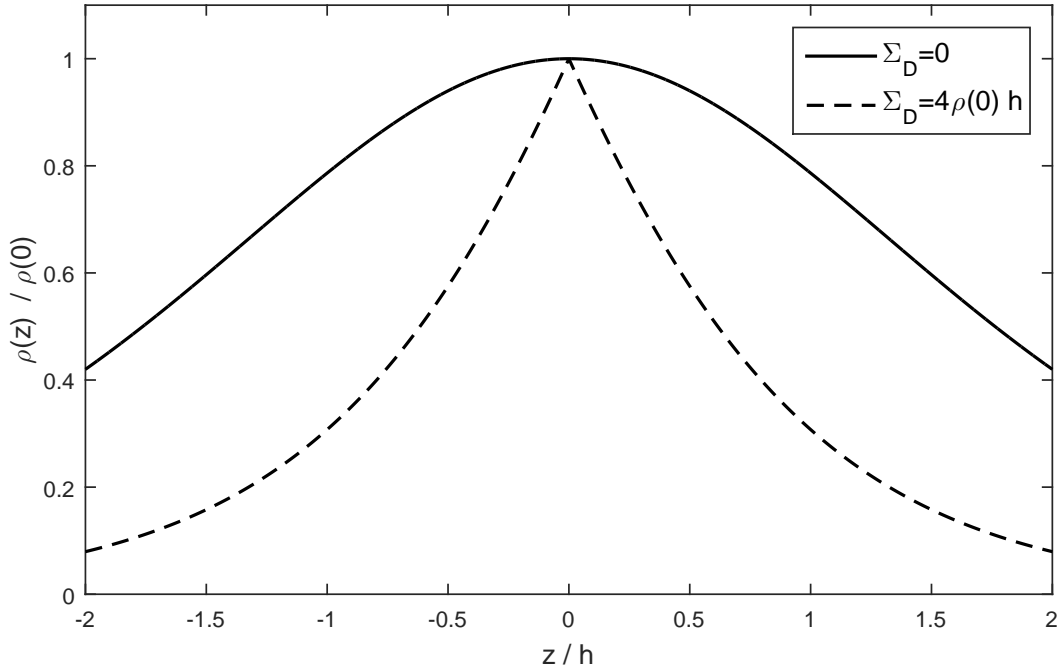


Fig. 1.— A plot of the exact solutions without and with a dark disk of $Q = 1$. The density is ‘pinched’ by the disk, in accordance with Equation 5.

Integrating (5) gives the surface density of the visible component as

$$\Sigma_{\text{vis}}(\Sigma_D) = \sqrt{\Sigma_{\text{vis}}(0)^2 + \Sigma_D^2} - \Sigma_D \quad (9)$$

where $\Sigma_{\text{vis}}(0) \equiv 4\rho_0 h$ is what the surface density would have been without the dark disk. This expression is monotonically decreasing with Σ_D .

Another way of explaining this is that the dark disk ‘pinches’ the visible matter disk, reducing its thickness H_{vis} . Since the surface density of the visible disk scales roughly as $\Sigma_{\text{vis}} \sim \rho_{\text{vis}} H_{\text{vis}}$, the effect of the dark disk is to reduce the total surface density for a given midplane density ρ_{vis} .

3. Analysis

Here we explain how we compare the surface densities of the various gas components estimated in the next section to those predicted by their midplane densities and velocity dispersions in order to place self-consistency constraints on the mass model. Section 2.1 explains how the presence of the dark disk decreases the surface density of each component if the midplane density is held fixed (as it is in a Poisson-Jeans solver). Thus, given fixed midplane densities, we can assign a probability to a model with any dark disk surface density Σ_D and scale height h_D based on how well the predicted surface densities Σ_i determined from the Poisson-Jeans solver match the observed values.

Starting with the midplane densities and dispersions of Section 4, we solved the Poisson-Jeans equation for Σ_D values between 0 and $24 M_{\odot} \text{pc}^{-2}$. Each time the Poisson-Jeans equation was solved, the density distributions were integrated to give the total surface densities of H_2 and HI . Each model was then assigned a probability, according to the chi-squared distribution with 2 degrees of freedom, based on the deviation of this surface density from the measured values. We did this using different central values and uncertainties for the midplane densities. Thus, for example, using $n_{\text{H}_2} = 0.19 \text{cm}^{-3}$, we would take $\rho_{\text{H}_2+\text{He}}(0) = 1.42 \times m_{\text{H}_2} \times 0.19 \text{cm}^{-3} = 0.013 M_{\odot} \text{pc}^{-3}$. If for a model with this value of $\rho_{\text{H}_2}(0)$ and with a certain dark disk surface density value of Σ_D we find an H_2 surface density $\Sigma_{\text{H}_2} = 1.0 M_{\odot} \text{pc}^{-2}$, then according to Section 4.1, we should assign this model a chi-squared value $\chi_{\text{H}_2}^2 = (1.0 - 1.3)^2 / \Delta_{\Sigma_{\text{H}_2}}^2$. We would then assign a probability to this model according to the Gaussian cumulative distribution, $p_{\text{H}_2} = \int d\chi \exp(-\chi^2/2) / \sqrt{2\pi}$, where the limits of integration are from $-\infty$ to $-\chi_{\text{H}_2}$ and χ_{H_2} to ∞ . We would similarly compute probabilities p_{HI} , p_{HII} , and a combined probability $p = p_{\text{H}_2} \times p_{\text{HI}} \times p_{\text{HII}}$. We note here that this is not the absolute probability of the model given the data; rather, it is the probability of the data given the model. We define a model for which the data is less probable than 5% to be excluded.

An important question is what to use for Δ_{Σ}^2 . There are two uncertainties here. Namely, 1) the uncertainty in the surface density measurements, $\Delta_{\hat{\Sigma}_i}$, and 2) the uncertainty in our output values of $\Sigma(\hat{\rho}_i, \Sigma_D)$, resulting from the uncertainty in the input midplane density measurements $\hat{\rho}_i$. Formally, this is $|\partial\Sigma_i/\partial\rho_i|\Delta_{\hat{\rho}_i}$. Assuming Gaussian distributions for the measurements $\hat{\Sigma}_i$ and $\hat{\rho}_i$, and a uniform prior for Σ_D , one can show that

$$p(\hat{\Sigma}_i, \hat{\rho}_i | \Sigma_D) \sim \int d\rho_i \exp\left(-\frac{(\hat{\Sigma}_i - \Sigma(\rho_i, \Sigma_D))^2}{2\Delta_{\hat{\Sigma}_i}^2}\right) \exp\left(-\frac{(\rho_i - \hat{\rho}_i)^2}{2\Delta_{\hat{\rho}_i}^2}\right) \quad (10)$$

where ρ_i are the true midplane densities, and that, expanding $\Sigma(\rho_i, \Sigma_D)$ to first order in ρ_i , this integrates to give an approximately Gaussian distribution for $\hat{\Sigma}_i - \Sigma(\hat{\rho}_i, \Sigma_D)$, with width

$$\Delta_{\Sigma_i} \simeq \sqrt{\Delta_{\hat{\Sigma}_i}^2 + \left(\frac{\partial \Sigma_i}{\partial \rho_i}\right)^2 \Delta_{\hat{\rho}_i}^2}. \quad (11)$$

We computed $|\partial \Sigma_i / \partial \rho_i|$ by sampling values of ρ_i and computing the output values Σ_i . The effect of the uncertainties in the vertical dispersions of the different components was also included in Δ_{Σ_i} in the same way as those in $\hat{\rho}_i$. The formula for Δ_{Σ_i} that we adopt (Equation 11) therefore contains an extra term under the square root to include this uncertainty:

$$\Delta_{\Sigma_i} \simeq \sqrt{\Delta_{\hat{\Sigma}_i}^2 + \left(\frac{\partial \Sigma_i}{\partial \rho_i}\right)^2 \Delta_{\hat{\rho}_i}^2 + \left(\frac{\partial \Sigma_i}{\partial \sigma_{i,\text{eff}}}\right)^2 \Delta_{\hat{\sigma}_{i,\text{eff}}}^2}. \quad (12)$$

4. Gas parameters

The purpose of this section is to determine accurate values for $\rho_i(0)$, σ_i , and Σ_i (midplane density, velocity dispersion, and surface density) for the different components of interstellar gas based on existing measurements. Using Equation 2, these can then be compared for a given dark disk model in order to check for self-consistency.

We now discuss in detail the various measurements of the gas parameters and the uncertainties in each. Our starting point is the Bahcall model used by Flynn et al. (2006, Table 2). These values are updated from the ones used in Holmberg & Flynn (2000). Values for the stellar components were updated using the values of McKee et al. (2015), and are shown in rows 5-15 in Table 2 of Kramer & Randall (2016).

In these models, the gas and stars are both separated into approximately isothermal components as in Bahcall (1984b), so that each component i is characterized by a midplane density ρ_{i0} and a vertical dispersion σ_i . Using only these values for all of the components, we can solve the Poisson-Jeans equation (4) for the system. A major difference between our model and that of Flynn et al. (2006) is that their gas midplane densities were fixed by the values needed to give the correct surface densities in accordance with the Poisson-Jeans equation. We, on the other hand, use measured values of the midplane densities as we explain in this section.

We explain the various literature values that were included in the determination of the gas parameters. We also compare these to the recent values of McKee et al. (2015). In Section 5, the analysis is conducted separately for the values we determine by combining the results in the literature and the values obtained solely from the recent paper by McKee et al. (2015).

4.1. Molecular hydrogen

We now explain the various measurements of the molecular hydrogen volume density and surface densities and how they are corrected. As molecular hydrogen cannot be observed directly, it must be inferred from the amount of CO present, derived from the intensity of the $J = 1 - 0$ transition photons. These are related by the so-called X -factor, defined by

$$N_{\text{H}_2} \equiv X W_{\text{CO}} \quad (13)$$

where $N_{\text{H}_2} = N_{\text{l.o.s.}}$ is the line-of-sight column density of H_2 molecules and W_{CO} is the total, velocity-integrated CO intensity along the line of sight (Draine 2011). Column densities perpendicular to the galactic plane can then be obtained by simple trigonometry:

$$N_{\perp} = N_{\text{l.o.s.}} \sin b \quad (14)$$

and volume densities can be obtained by dividing the intensity density in velocity space dW_{CO}/dv by the rotation curve gradient dv/dR , or by estimating the distance along the line of sight using other means. The volume and surface densities can also both be found by fitting an assumed distribution to measurements of the gas' vertical scale height Δz . Surface densities can then be given, for example, by

$$\Sigma_{\text{H}_2} = m_{\text{H}_2} N_{\perp, \text{H}_2} = m_{\text{H}_2} X W_{\text{CO}} \sin b. \quad (15)$$

On the other hand, a certain reference may not be measuring surface density directly. Instead, they may be measuring the emissivity,

$$J(\mathbf{r}) \equiv \frac{dW_{\text{CO}}}{dr} \quad (16)$$

from which, according to Equation 13, we can obtain the volume density as

$$n(\mathbf{r}) = X J(\mathbf{r}). \quad (17)$$

If the authors also measured the vertical (z -direction) distribution of the molecular hydrogen, then the surface mass density can be obtained according to

$$\Sigma_{\text{H}_2} = m_{\text{H}_2} \int n_{\text{H}_2}(z) dz. \quad (18)$$

For example, the full width at half maximum (FWHM) of the molecular hydrogen distribution gives the surface density as

$$\Sigma_{\text{H}_2} = m_{\text{H}_2} C_{\text{shape}} n_{\text{H}_2}(0) \times \text{FWHM} \quad (19)$$

where C_{shape} is given by 1.06, 1.13, or 1.44 for a Gaussian, sech^2 , or exponential profile respectively. For our calculations, we used

$$C_{\text{shape}} = 1.10 \quad (20)$$

as a reasonable estimate for the shape of the distribution.

In the literature, mass values are often quoted including the associated helium, metals, and other gaseous components such as CO, etc. The amount of helium accompanying the hydrogen is typically assumed in the range 36-40% of the hydrogen alone by mass (Kulkarni & Heiles 1987; Bronfman et al. 1988). Including other gas components increases this number to about 42% (Ferrière 2001). Thus, the total mass of any component of the ISM should be about 1.42 times the mass of its hydrogen. These will be distinguished by using, e.g. Σ_{H_2} , $\Sigma_{\text{H}_2+\text{He}}$ to refer to the bare values and the values including their associated helium respectively. Thus,

$$\Sigma_{\text{H}_2+\text{He}} = 1.42 \Sigma_{\text{H}_2}. \quad (21)$$

Note that Binney & Merrifield (1998, p.662) did not include helium in the total ISM mass. Also Read (2014) did not distinguish between HI results including and not including helium.

We now explain how we obtain midplane volume densities $n_{\text{H}_2}(z=0)$ and surface densities $\Sigma_{\text{H}_2+\text{He}}$ from the various references in the literature. Bronfman et al. (1988) measured the molecular hydrogen over different radii within the solar circle. Their data are shown as one of the data sets in Figure 2. Averaging the values from the Northern and Southern Galactic plane in Table 4 of the latter, we find, for the measurements closest to the Sun, $\Sigma_{\text{H}_2} = 2.2 M_{\odot}\text{pc}^{-2}$ and $n_{\text{H}_2} = 0.2 \text{cm}^{-3}$. Since surface densities depend only on the total integrated intensity along the line of sight, they are independent of the value of R_{\odot} , the Sun’s radial position from the center of the Galaxy. On the other hand, it follows from this that old values for volume densities (which scale as R_{\odot}^{-1}) must be rescaled by $R_{\odot,\text{old}}/R_{\odot,\text{new}}$ (Scoville & Sanders 1987, p.31). Since Bronfman et al. used the old value $R_{\odot} = 10 \text{kpc}$, this value needs to be rescaled by $(0.833)^{-1}$ to take into account the new value of $R_{\odot} = 8.33 \pm 0.35 \text{kpc}$ (Gillessen et al. 2009). They also used an X -factor of $X = 2.8 \times 10^{20} \text{cm}^{-2} (\text{K}^{-1} \text{km s}^{-1})^{-1}$. We correct this using a more recent value of $X = 1.8 \pm 0.3 \times 10^{20} \text{cm}^{-2} (\text{K}^{-1} \text{km s}^{-1})^{-1}$, obtained by Dame, Hartmann, & Thaddeus (2001). The most recent value of X , obtained by Okumura & Kamae (2009), is $X = 1.76 \pm 0.04 \times 10^{20} \text{cm}^{-2} (\text{K}^{-1} \text{km s}^{-1})^{-1}$, although the value of Dame et al. that we use is still cited by Draine (2011) as the most reliable. These corrections give $n_{\text{H}_2} = 0.15 M_{\odot}\text{pc}^{-3}$ and $\Sigma_{\text{H}_2} = 1.4 M_{\odot}\text{pc}^{-2}$. Including helium gives $\Sigma_{\text{H}_2+\text{He}} = 2.0 M_{\odot}\text{pc}^{-2}$.

On the other hand, Clemens, Sanders, & Scoville (1988), found the local CO emissivity $J = dW_{\text{CO}}/dr$ in the first galactic quadrant for radii through R_{\odot} . For $R < R_{\odot}$ and $R > R_{\odot}$ respectively, they found these to be $J = 3.1$ and $2.3 \text{K km s}^{-1} \text{kpc}^{-1}$, which, using $X = 1.8 \times 10^{20} \text{cm}^{-2} (\text{K}^{-1} \text{km s}^{-1})^{-1}$, and rescaling for R_{\odot} by $(0.833)^{-1}$, gives interpolated density $n_{\text{H}_2}(R_{\odot}) = 0.19 \text{cm}^{-3}$. Using their FWHM measurements for H_2 , we can convert their measurements to surface density values according to Equation 19. As before, the surface density values are independent of R_{\odot} . We have, interpolating to R_{\odot} , $\Sigma_{\text{H}_2+\text{He}} = 1.1 M_{\odot}\text{pc}^{-2}$. The rescaled data are shown in Figure 2.

Another measurement is provided by Burton & Gordon (1978), who had already measured Galactic CO emissivity $J = dW_{\text{CO}}/dr$ between $R \sim 2 - 16 \text{kpc}$, assuming $R_{\odot} = 10 \text{kpc}$, from which we obtain $n_{\text{H}_2}(R)$ after correcting for R_{\odot} , shown in Figure 2. Interpolating linearly, this

gives $n(R_\odot) = 0.31 \text{ cm}^{-3}$. Sanders, Solomon, & Scoville (1984) also measured CO in the first and second Galactic quadrants within and outside the solar circle. They used the values $R_\odot = 10 \text{ kpc}$ and $X = 3.6 \times 10^{20} \text{ cm}^{-2} (\text{K}^{-1} \text{ km s}^{-1})^{-1}$. Their results for both volume and surface density, corrected to $R_\odot = 8.33 \text{ kpc}$ and $X = 1.8 \times 10^{20} \text{ cm}^{-2} (\text{K}^{-1} \text{ km s}^{-1})^{-1}$, are also shown in Figure 2. In particular, after rescaling and interpolating their volume densities, we have $n(0.95R_\odot) = 0.39 \text{ cm}^{-3}$. For surface density, we obtain $\Sigma_{\text{H}_2+\text{He}} = 2.7 M_\odot \text{ pc}^{-2}$. This is the highest value in the literature. Grabelsky et al. (1987) also measured CO in the outer Galaxy, which, with a 1.8/2.8 correction factor for X , as well as correcting R_\odot from 10 to 8.33 kpc, their results near the Sun read $n(1.05R_\odot) = 0.14 \text{ cm}^{-3}$ and $\Sigma_{\text{H}_2}(1.05R_\odot) = 1.4 M_\odot \text{ pc}^{-2}$. Digel (1991) also measured H_2 in the outer Galaxy. Using his results, we find $n(1.06R_\odot) = 0.13 \text{ cm}^{-3}$ and $\Sigma_{\text{H}_2}(1.06R_\odot) = 2.1 M_\odot \text{ pc}^{-2}$.

Dame et al. (1987), by directly observing clouds within 1 kpc of the Sun only, found local volume density $n_{\text{H}_2} = 0.10 \text{ cm}^{-3}$ and surface density $\Sigma_{\text{H}_2+\text{He}} = 1.3 M_\odot \text{ pc}^{-2}$, which, correcting for $X = 2.7$ to $1.8 \times 10^{20} \text{ cm}^{-2} (\text{K}^{-1} \text{ km s}^{-1})^{-1}$, gives 0.08 cm^{-3} and $0.87 M_\odot \text{ pc}^{-2}$. This volume density is lower than many other measurements, and may represent a local fluctuation in the Solar region on a larger scale than the Local Bubble. On the other hand, their surface density value is not the lowest. Luna et al. (2006), using $X = 1.56 \times 10^{20} \text{ cm}^{-2} (\text{K}^{-1} \text{ km s}^{-1})^{-1}$, found $\Sigma_{\text{H}_2+\text{He}}(0.975R_\odot) = 0.24 M_\odot \text{ pc}^{-2}$. Correcting for X gives $0.29 M_\odot \text{ pc}^{-2}$, which is the lowest value in the literature. However, they admit that their values beyond $0.875 R_\odot$ are uncertain. Another determination from 2006 (Nakanishi & Sofue 2006) gives, after interpolation, $n_{\text{H}_2}(R_\odot) = 0.17 \text{ cm}^{-3}$ and $\Sigma_{\text{H}_2}(R_\odot) = 1.4 M_\odot \text{ pc}^{-2}$, or $\Sigma_{\text{H}_2}(R_\odot) = 2.0 M_\odot \text{ pc}^{-2}$.

Figure 2 shows the various measurements described here, as well as the overall average and standard error. Although not all measurements are equally certain, in computing average values for n_{H_2} and Σ_{H_2} we treated all measurements with equal weight. We estimated the resulting uncertainty as the standard deviation divided by the the square root of the number of measurements available at each R . We found the mean values and standard errors of volume and surface densities near the Sun to be

$$n_{\text{H}_2}(R_\odot) = 0.19 \pm 0.03 \text{ cm}^{-3} \quad (22)$$

$$\Sigma_{\text{H}_2+\text{He}}(R_\odot) = 1.55 \pm 0.32 M_\odot \text{ pc}^{-2}. \quad (23)$$

This analysis has not yet taken into account the more recent observations of a significant component of molecular gas that is not associated with CO (Heyer & Dame 2015; Hessman 2015). Planck Collaboration et al. (2011) estimates this “dark gas” density to be 118% that of the CO-associated H_2 . Pineda et al. (2013), on the other hand, found roughly 40% at Solar radius. We therefore include the dark molecular gas with a mean value of 79% and with an uncertainty of 39%. This gives total molecular gas estimates of

$$n_{\text{H}_2+\text{DG}}(R_\odot) = 0.34 \pm 0.09 \text{ cm}^{-3} \quad (24)$$

$$\Sigma_{\text{H}_2+\text{He}+\text{DG}}(R_\odot) = 2.8 \pm 0.8 M_\odot \text{ pc}^{-2} \quad (25)$$

which are the values we assume for our analysis. It should be noted, however, that in propagating the errors for dark gas, n_{H_2} and $\Sigma_{\text{H}_2+\text{He}}$ always vary together. We take this into account in the

statistical analysis by considering only the error on the ratio Σ/ρ . The same would apply to the error in X_{CO} although this error is much smaller.

Besides the molecular hydrogen’s volume density n_{H_2} and surface density Σ_{H_2} , another important quantity is its cloud-cloud velocity dispersion σ_{H_2} , since this is one of the inputs in the Poisson-Jeans equation. The velocity dispersions of the molecular clouds containing H_2 can be inferred from that of their CO, which was found by Liszt & Burton (1983) to be $\sigma_{\text{H}_2} = 4.2 \pm 0.5 \text{ km s}^{-1}$. Belfort & Crovisier (1984) found $\sigma_{\text{CO}} = \sigma_{\text{H}_2} = 3.6 \pm 0.2 \text{ km s}^{-1}$. Scoville & Sanders (1987) found $\sigma_{\text{H}_2} = 3.8 \pm 2 \text{ km s}^{-1}$. The weighted average of these is approximately given by

$$\sigma_{\text{H}_2} = 3.7 \pm 0.2 \text{ km s}^{-1}. \quad (26)$$

4.2. The Atomic Hydrogen

We now discuss the various measurements of atomic hydrogen HI volume density $n_{\text{HI}}(z)$ and surface density Σ_{HI} . These typically are made by observing emissions of hydrogen’s 21 cm hyperfine transition. Kulkarni & Heiles (1987) estimate an HI surface density of $8.2 M_{\odot}\text{pc}^{-2}$ near the Sun. They separate HI into the Cold Neutral Medium (CNM) and Warm Neutral Medium (WNM).

Dickey & Lockman (1990), summarizing several earlier studies, describe the Galactic HI as having approximately constant properties over the range $4 \text{ kpc} < R < 8 \text{ kpc}$. Their best estimate for the HI parameters over this range is a combination of subcomponents, one thin Gaussian component with central density $n(0) = 0.40 \text{ cm}^{-3}$ and FWHM = 212 pc (and surface density $2.2 M_{\odot}\text{pc}^{-2}$), which we identify with the CNM, and a thicker component with central density $n(0) = 0.17 \text{ cm}^{-3}$ and surface density $2.8 M_{\odot}\text{pc}^{-2}$, which we identify as the WNM. This gives a total of $\Sigma_{\text{HI}} = 5.0 M_{\odot}\text{pc}^{-2}$, or $\Sigma_{\text{HI+He}} = 7.1 M_{\odot}\text{pc}^{-2}$. Another measurement is provided by Burton & Gordon (1978), who measured volume densities for $R \sim 2 - 16 \text{ kpc}$. We interpolate their data (and correct for $R_{\odot} = 10 \text{ kpc} \rightarrow 8.33 \text{ kpc}$) to obtain $n_{\text{HI}} = 0.49 \text{ cm}^{-3}$. Although they did not determine surface densities, we can estimate them by assuming a single Gaussian component with FWHM given Dickey & Lockman (220 - 230 pc). A better estimate is perhaps obtained by assuming, rather than a Gaussian distribution, a distribution with the same shape as Dickey & Lockman. This amounts to assuming an effective Gaussian FWHM of $\sim 330 \text{ pc}$. This gives a surface density near the Sun of $\Sigma_{\text{HI+He}} = 5.9 M_{\odot}\text{pc}^{-2}$. Liszt (1992), however, argues that the midplane density of Dickey & Lockman was artificially enhanced to give the correct surface density. He measures midplane density $n_{\text{HI}} = 0.41 \text{ cm}^{-3}$, which, assuming as for Burton & Gordon a Gaussian distribution with effective FWHM 330 pc, gives a surface density of only $\Sigma_{\text{HI+He}} = 5.1 M_{\odot}\text{pc}^{-2}$. Nakanishi & Sofue (2003) also measured the Galactic HI, from the Galactic center out to $\sim 25 \text{ kpc}$. Their results are shown in Figure 3. Interpolating to R_{\odot} , we have $n_{\text{HI}}(R_{\odot}) = 0.28 \text{ cm}^{-3}$ and $\Sigma_{\text{HI+He}} = 5.9 M_{\odot}\text{pc}^{-2}$, in agreement with the value of Burton & Gordon.

On the other hand, there are several authors who report much larger mass parameters for Galactic HI. They are Wouterloot et al. (1990) and Kalberla & Dedes (2008). Wouterloot et al. used 21 cm observations from outside the Solar circle. Their data are shown in Figure 3. Closest to the Sun, their data show $\Sigma_{\text{HI+He}}(1.06R_{\odot}) = 8.6 M_{\odot}\text{pc}^{-2}$ with a FWHM of 300 pc. This corresponds to a midplane density of roughly $n_{\text{HI}} = 0.73 \text{ cm}^{-3}$. The Kalberla & Dedes data (also shown in Figure 3) show $\Sigma_{\text{HI+He}} \simeq 10 M_{\odot}\text{pc}^{-2}$. A more refined estimate gives $\Sigma_{\text{HI+He}} \simeq 9 M_{\odot}\text{pc}^{-2}$ (McKee et al. 2015). This is consistent with a midplane density of roughly 0.8 cm^{-3} . This is much higher than the value of Kalberla & Kerp (1998), who obtained $n_{\text{CNM}} = 0.3 \text{ cm}^{-3}$ and $n_{\text{WNM}} = 0.1 \text{ cm}^{-3}$. However, there is reason to expect a relatively high HI midplane density. Based on extinction studies, Bohlin, Savage, & Drake (1978) find a total hydrogen nucleus density $2n_{\text{H}_2} + n_{\text{HI}} = 1.15 \text{ cm}^{-3}$. Updating this for the newer value of the Galactocentric radius of the Sun R_{\odot} as in Section 4.1, we have $2n_{\text{H}_2} + n_{\text{HI}} = 1.38 \text{ cm}^{-3}$. According to the average midplane density determined for molecular hydrogen in Section 4.1, $n_{\text{H}_2} = 0.19 \pm 0.03 \text{ cm}^{-3}$, and including an additional $0.15 \pm 0.07 \text{ cm}^{-3}$ for the dark molecular hydrogen, we therefore expect an atomic hydrogen density $n_{\text{HI}} = 0.70 \pm 0.18 \text{ cm}^{-3}$. Optical thickness corrections, which we explain below, increase this number to 0.84 cm^{-3} . The results are shown in Figure 3. As in the case of molecular hydrogen, all measurements were treated with equal weight and the uncertainty was estimated as the standard error at each R .

Combining all these results, we have, in the absence of optical thickness corrections,

$$n_{\text{HI}}(R_{\odot}) = 0.53 \pm 0.10 \text{ cm}^{-3} \quad (27)$$

$$\Sigma_{\text{HI+He}}(R_{\odot}) = 7.2 \pm 0.7 M_{\odot}\text{pc}^{-2}. \quad (28)$$

In the Dickey & Lockman (1990) model, 70% of this HI midplane density is in CNM and the remaining 30% is WNM. In Kalberla & Kerp (1998), the numbers are 75% and 25%. We will take the average of these two results, 72.5% and 27.5%, which give $n_{\text{CNM}} = 0.38 \text{ cm}^{-3}$ and $n_{\text{WNM}} = 0.15 \text{ cm}^{-3}$.

McKee et al. (2015) pointed out that these numbers must be corrected for the optical depth of the CNM. Assuming the CNM to be optically thin leads to an underestimation of the CNM column density by a factor \mathcal{R}_{CNM} . McKee et al. (2015) estimate this factor to be $\mathcal{R}_{\text{CNM}} = 1.46$, which they translate, for the total HI column density, to $\mathcal{R}_{\text{HI}} = 1.20$. Correcting for this gives

$$n_{\text{CNM}} \simeq 0.56 \text{ cm}^{-3} \quad (29)$$

$$n_{\text{WNM}} \simeq 0.15 \text{ cm}^{-3}. \quad (30)$$

with totals

$$n_{\text{HI}}(R_{\odot}) = 0.71 \pm 0.13 \text{ cm}^{-3} \quad (31)$$

$$\Sigma_{\text{HI+He}}(R_{\odot}) = 8.6 \pm 0.8 M_{\odot}\text{pc}^{-2}. \quad (32)$$

which we use for this analysis.

On the other hand, McKee et al. (2015) argues that the model of Heiles et al. (1981) is more accurate, and recommends increasing the amount of HI in the ISM by a factor of 7.45/6.2.

McKee et al. (2015)’s values are therefore $n_{\text{CNM}} = 0.69 \text{ cm}^{-3}$, $n_{\text{WNM}} = 0.21 \text{ cm}^{-3}$, $n_{\text{HI}} = 0.90 \text{ cm}^{-3}$, and $\Sigma_{\text{HI}} = 10.0 \pm 1.5 M_{\odot} \text{ pc}^{-2}$. Although these numbers are different from our average of conventional measurements (Equations 29-32), it agrees with the extinction result of Bohlin et al. (1978) mentioned above once the latter is corrected for the optical depth of the CNM. To account for any discrepancy, we perform our analysis separately using the values of Equations 29 to 32 and the results of McKee et al. (2015). We present both results in Section 5.

For the atomic hydrogen’s velocity dispersion, Heiles & Troland (2003), found $\sigma_{\text{CNM}} = 7.1 \text{ km s}^{-1}$ and $\sigma_{\text{WNM}} = 11.4 \text{ km s}^{-1}$, while Kalberla & Dedes (2008) found $\sigma_{\text{CNM}} = 6.1 \text{ km s}^{-1}$ and $\sigma_{\text{WNM}} = 14.8 \text{ km s}^{-1}$. Earlier, Belfort & Crovisier (1984) measured $\sigma_{\text{HI}} = 6.9 \pm 0.4 \text{ km s}^{-1}$, and Dickey & Lockman (1990) found $\sigma_{\text{HI}} = 7.0 \text{ km s}^{-1}$ but did not specify if the gas was CNM or WNM. Since these are comparable to more recent measurements of the CNM component of HI, we assume both of these to correspond to σ_{CNM} . The averages of these values are

$$\sigma_{\text{CNM}} = 6.8 \pm 0.5 \text{ km s}^{-1} \quad (33)$$

$$\sigma_{\text{WNM}} = 13.1 \pm 2.4 \text{ km s}^{-1}. \quad (34)$$

4.3. Ionized Hydrogen

Besides the H_2 and the two types of HI (CNM and WNM), there is a fourth, warm, ionized component of interstellar hydrogen, denoted HII. Holmberg & Flynn (2000) and Flynn et al. (2006) included this component. Binney & Merrifield (1998) did not include the ionized component in the value for Σ_{ISM} , possibly because of its very large scale height. Its density is typically obtained by measuring the dispersion of pulsar signals that have passed through the HII clouds. The time delay for a pulse of a given frequency is proportional to the dispersion measure

$$\text{DM} = \int n_e ds \quad (35)$$

where the integral is performed along the line of sight to the pulsar, and where n_e is the electron number density, equal to the number density of ionized gas. The dispersion measure perpendicular to the plane of the Galaxy, $\text{DM}_{\perp} = \text{DM} / \sin b$, therefore corresponds to the half surface density $1/2 \Sigma_{\text{HII}}$. Fitting a spatial distribution (e.g. exponential profile), provides midplane density information. For its midplane density, Kulkarni & Heiles (1987) found $n_{\text{HII}} = 0.030 \text{ cm}^{-3}$; Cordes et al. (1991) found $n_{\text{HII}} = 0.024 \text{ cm}^{-3}$; Reynolds (1991) found $n_{\text{HII}} = 0.040 \text{ cm}^{-3}$. The average of these values is

$$n_{\text{HII}} = 0.031 \pm 0.008 \text{ cm}^{-3}. \quad (36)$$

This agrees with the traditional model of Taylor & Cordes (1993), refined by Cordes & Lazio (2002), who found a midplane density of

$$n_{\text{HII}} = 0.034 \text{ cm}^{-3}. \quad (37)$$

For the HII surface density, Reynolds (1992) reports $\Sigma_{\text{HII+He}} = 1.57 M_{\odot}\text{pc}^{-2}$. This is slightly higher than what was found by Taylor & Cordes (1993), who found a one-sided column density $1/2 N_{\perp,\text{HII}} = 16.5 \text{ cm}^{-3} \text{ pc}$, or $\Sigma_{\text{HII+He}} = 1.1 M_{\odot}\text{pc}^{-2}$, but it is slightly lower than the more recent value of Cordes & Lazio (2002), who found $1/2 N_{\perp,\text{HII}} = 33 \text{ cm}^{-3} \text{ pc}$, or $\Sigma_{\text{HII+He}} = 2.3 M_{\odot}\text{pc}^{-2}$. Assuming an exponential profile, with the scale height of 0.9 kpc of Taylor & Cordes (1993), the Reynolds (1992) result agrees with the midplane densities of Equations 36 and 37. However, Gaensler et al. (2008) argued for a scale height of 1.8 kpc that a distribution with midplane density of

$$n_{\text{HII}} = 0.014 \text{ cm}^{-3}. \quad (38)$$

Similarly, Schnitzeler (2012) also argues for large scale heights of ~ 1.4 kpc. For DM values between 20 and $30 \text{ cm}^{-3} \text{ pc}$, this gives a midplane density of $\sim 0.015 \text{ cm}^{-3} \text{ pc}$, as preferred by McKee et al. (2015). As we explain in Section 5, we do not find our model to be consistent with these large scale heights, even without a dark disk. We therefore do not use HII parameters in this paper as a constraint.

For its velocity dispersion, Holmberg & Flynn (2000) used the value $\sigma_{\text{HII}} = 40 \text{ km s}^{-1}$. This value seems to have been inferred from scale height measurements of the electrons associated with this ionized gas from Kulkarni & Heiles (1987). From the data in Reynolds (1985), however, we find a turbulent component to the dispersion of only $\sigma_{\text{HII}} = 21 \pm 5 \text{ km s}^{-1}$. On the other hand, temperatures between 8,000 K and 20,000 K give a thermal contribution of $\sigma_{\text{HII,thermal}} = \sqrt{2.1 k_B T / m_p} \simeq 12 - 19 \text{ km s}^{-1}$ (Ferrière 2001, p.14). Summing these in quadrature gives $\sigma_{\text{HII}} = 25 - 29 \text{ km s}^{-1}$. As we will explain in Section 4.4, including magnetic and cosmic ray pressure contributions pushes this up to 42 km s^{-1} . Similarly, Kalberla (2003) also finds $\sigma_{\text{HII}} = 27 \text{ km s}^{-1}$ while assuming $p_{\text{mag}} = p_{\text{cr}} = 1/3 p_{\text{turb}}$, for a total effective dispersion of 35 km s^{-1} but did not include a thermal contribution. This gives an average total effective dispersion of $39 \pm 4 \text{ km s}^{-1}$, which, removing magnetic, cosmic ray, and thermal contributions, gives a turbulent dispersion of $\sigma_{\text{HII}} = 22 \pm 3 \text{ km s}^{-1}$.

The new gas parameter estimates, obtained in this work by incorporating a broad range of literature values, are summarized in Table 1 alongside the old (Flynn et al. 2006) values. The values of McKee et al. (2015) are also included for comparison.

4.4. Other Forces

Boulares & Cox (1990) considered the effect of magnetic forces and cosmic ray pressure on the interstellar gas. The effect of the magnetic field is a contribution to the force per unit volume on the i^{th} component of the gas:

$$\mathbf{f}_i = \mathbf{J}_i \times \mathbf{B} \quad (39)$$

Table 1: Old values (Flynn et al. 2006) and new values (including all the references mentioned in Section 4) estimated in this paper. We also include the values of McKee et al. (2015).

Component	Flynn et al. (2006)	This reference	McKee et al. (2015)
	$n(0)$ [cm ⁻³]	$n(0)$ [cm ⁻³]	$n(0)$ [cm ⁻³]
H ₂ *	0.30	0.19	0.15
HI(CNM)	0.46	0.56	0.69
HI(WNM)	0.34	0.15	0.21
HII	0.03	0.03	0.0154

* does not include dark molecular gas

where \mathbf{J}_i is the current density associated with gas component i , \mathbf{B}_i is the magnetic induction field due to component i , and where

$$\mathbf{B} \equiv \sum_i \mathbf{B}_i \quad (40)$$

is the total magnetic field from all the gas components. Using Ampere’s law, we can rewrite the z -component of the force as

$$f_{zi} = \frac{1}{\mu_0} ((\nabla \times \mathbf{B}_i) \times \mathbf{B})_z \quad (41)$$

$$= \frac{1}{\mu_0} (\mathbf{B} \cdot \text{div}) \mathbf{B}_{iz} - \frac{1}{\mu_0} \mathbf{B} \cdot \frac{\partial \mathbf{B}_i}{\partial z} \quad (42)$$

Since according to Parker (1966), the magnetic field is, on average, parallel to the plane of the Galaxy, ($B_z = 0$) we will make the approximation that the first term vanishes in equilibrium. The second term couples each gas component to the remaining components, since \mathbf{B} represents the total magnetic field. However, summing all components, we have

$$f_z \equiv \sum_i f_{zi} = -\frac{1}{\mu_0} \mathbf{B} \cdot \frac{\partial \mathbf{B}}{\partial z} \quad (43)$$

$$= -\frac{\partial}{\partial z} \left(\frac{B^2}{2\mu_0} \right). \quad (44)$$

We recognize the form of this expression as the gradient of the magnetic pressure $p_B = B^2/2\mu_0$. To include this effect in the Poisson-Jeans Equation, we note that the first term on the left-hand-side of Equation 1 has the interpretation (up to an overall mass factor) as the gradient of a ‘vertical pressure’. This pressure term is a correct description of a population of stars or of gas clouds. In a warm gas, this term has the interpretation as the turbulent pressure of the gas. However, in this case, one also needs to take into account the thermal pressure of the gas

$$p_{\text{thermal}} = c_i n_i k_B T_i \quad (45)$$

where c_i is a factor that takes into account the degree of ionization of the gas, and $n_i = \rho_i/m_p$ is the number density of the gas atoms. The correct Poisson-Jeans equation in this case therefore

reads

$$\frac{\partial}{\partial z}(\rho_i \sigma_i^2 + \rho_i c_i k_B T_i) + \rho_i \frac{\partial \Phi}{\partial z} = 0. \quad (46)$$

If we define a ‘thermal dispersion’ as

$$\sigma_{i,T}^2 \equiv c_i k_B T_i \quad (47)$$

then we can rewrite this as

$$\frac{\partial}{\partial z}(\rho_i(\sigma_i^2 + \sigma_{i,T}^2)) + \rho_i \frac{\partial \Phi}{\partial z} = 0. \quad (48)$$

Clearly, to account for the magnetic pressure, we would include the average of the magnetic pressure term in precisely the same manner:

$$\sum_i \frac{\partial}{\partial z}(\rho_i(\sigma_i^2 + \sigma_{i,T}^2)) + \frac{\partial}{\partial z} \left\langle \frac{B^2}{2\mu_0} \right\rangle + \rho \frac{\partial \Phi}{\partial z} = 0. \quad (49)$$

where ρ is the total mass density of the gas. In the following subsections, we describe how we model this magnetic pressure term.

4.4.1. Magnetic Pressure: Thermal Scaling Model

An important phenomenon noted by Parker (1966) is that the magnetic field B is confined by the weight of the gas through which it penetrates. We therefore would like to solve this equation by following Parker in assuming that the magnetic pressure is proportional to the thermal pressure term, $p_i = \rho_i c_i k_B T_i$. Since each gas component contributes to the total thermal pressure with a different temperature T_i , we write:

$$\left\langle \frac{B^2(z)}{2\mu_0} \right\rangle = \alpha \sum_i \rho_i(z) \sigma_{i,T}^2 \quad (50)$$

$$= \sum_i \rho_i(z) \sigma_{i,B}^2 \quad (51)$$

where α is a proportionality constant fixed by $\langle B^2(0) \rangle$ and $\sum_i \sigma_{i,T}^2$, and where we have defined the ‘magnetic dispersion’ $\sigma_{i,B}^2 \equiv \alpha \sigma_{i,T}^2$ i.e. the effective dispersion arising from the magnetic pressure. The Poisson-Jeans equation then reads

$$\sum_i \frac{\partial}{\partial z} \left(\rho_i (\sigma_i^2 + \sigma_{i,T}^2 + \sigma_{i,B}^2) \right) + \rho \frac{\partial \Phi}{\partial z} = 0. \quad (52)$$

The above equation admits many solutions. However, we will assume that the unsummed equation

$$\frac{\partial}{\partial z} \left(\rho_i (\sigma_i^2 + \sigma_{i,T}^2 + \sigma_{i,B}^2) \right) + \rho_i \frac{\partial \Phi}{\partial z} = 0. \quad (53)$$

holds for each component individually. This amounts to assuming that all gas components confine the magnetic field equally. Other solutions can be found by substituting $\sigma_{i,B}^2 \rightarrow \sigma_{i,B}^2 + S_i(z)$, such that $\sum_i \rho_i(z) S_i(z) = 0$. However, if we restrict our analysis to ‘isothermal’ solutions (constant

$\sigma_{i,B}^2$) the solution $S_i = 0$ will be unique. We can also include the effects of cosmic ray pressure in a similar way, by assuming that the partial cosmic ray pressure is also proportional to the density

$$p_{i,\text{cr}}(z) = \rho_i(z) \sigma_{i,\text{cr}}^2 \quad (54)$$

and where $\sigma_{i,\text{cr}}^2 = \beta \sigma_{i,T}^2$ for some other constant β . The Poisson-Jeans Equation then reads

$$\frac{\partial}{\partial z}(\rho_i \sigma_{i,\text{eff}}^2) = \sum_i \frac{\partial}{\partial z} \left(\rho_i (\sigma_i^2 + \sigma_{i,T}^2 + \sigma_{i,B}^2 + \sigma_{i,\text{cr}}^2) \right) + \rho \frac{\partial \Phi}{\partial z} = 0, \quad (55)$$

where we have defined

$$\sigma_{i,\text{eff}}^2 = \sigma_i^2 + \sigma_{i,T}^2 + \sigma_{i,B}^2 + \sigma_{i,\text{cr}}^2. \quad (56)$$

The solution to the Poisson-Jeans Equation for each component will then be

$$\rho_i(z) = \rho_i(0) \exp \left(-\frac{\Phi(z)}{\sigma_{i,\text{eff}}^2} \right). \quad (57)$$

Note that since the pressure is additive, the dispersions add in quadrature. Boulares & Cox (1990) estimate for the magnetic pressure $p_B \simeq (0.4 - 1.4) \times 10^{-12} \text{ dyn cm}^{-2}$. For the cosmic ray pressure, they estimate $p_{\text{cr}} \simeq (0.8 - 1.6) \times 10^{-12} \text{ dyn cm}^{-2}$. The dispersions for each component are shown in Table 2 for comparison, as well as the effective dispersions in this model.

There is, however, no clear evidence to support this model. Although $p_{\text{mag}} \propto p_{\text{cr}} \propto nk_B T$ has been assumed in the past (Parker 1966), this was when the entire gas was treated as a single component. Equation 50, however, is much more specific. We therefore supplement this model with a second model in the next subsection for comparison.

4.4.2. Magnetic Pressure: Warm Equipartition Model

Here we describe a second possible model to describe the magnetic and cosmic ray pressures in the interstellar medium. Namely, it has been observed that within the CNM, energy densities in magnetic fields and in turbulence are often roughly equal (Heiles & Troland 2003; Heiles & Crutcher 2005). Although the ratio between these energies is observed to vary greatly over different molecular

Table 2: Intrinsic and effective dispersions for ISM components

Component	σ [km s ⁻¹]	σ_T [km s ⁻¹]	σ_B [km s ⁻¹]	σ_{cr} [km s ⁻¹]	σ_{eff} (thermal scaling) [km s ⁻¹]	σ_{eff} (warm equipartition) [km s ⁻¹]
H ₂	3.7	0.2	0.3	0.3	3.7	6.4
HI(CNM)	6.8	0.8	1.2	1.3	7.1	11.8
HI(WNM)	13.1	6.7	10.3	10.9	21	23.7
HII	22	11.8	18.1	19	36.2	39.9

clouds, this so-called “energy equipartition” seems to be obeyed on average. Physically, this happens because the turbulence amplifies the magnetic field until it becomes strong enough to dissipate through van Alfvén waves. Similarly, we expect magnetic fields to trap cosmic rays within the gas until they become too dense and begin to escape. We might therefore expect the cosmic ray and magnetic field energy densities to be similar. For these reasons, an alternative to the first model (Equation 50) would be to assume equipartition of pressure between turbulence, magnetic fields, and cosmic rays:

$$\sigma_i^2 = \sigma_{i,B}^2 = \sigma_{i,cr}^2 \quad (58)$$

for each component i . The effective dispersion, which is the sum of turbulent, magnetic, cosmic ray, and thermal contributions, would then be

$$\sigma_{i,\text{eff}}^2 = \sigma_i^2 + \sigma_{i,B}^2 + \sigma_{i,cr}^2 + \sigma_{i,T}^2 \quad (59)$$

$$\simeq 3\sigma_i^2 + \sigma_{i,T}^2 \quad (60)$$

for each component. One important factor that we should not overlook here, however, is that the molecular hydrogen and CNM condense to form clouds. Thus, although turbulence, magnetic fields, and cosmic rays may affect the size of the individual clouds, we expect the overall scale height of the cold components to be determined only by the cloud-cloud dispersion and not by these forces. We therefore assume Equations 58-60 only for the warm components WNM and HII. For the cold components (H_2 and CNM), we assume $\sigma_{i,\text{eff}} = \sigma_i$. We perform calculations separately for the two different magnetic field and cosmic ray models. The effective dispersions in both models are shown in Table 2. As we will see, the results from both models are in good agreement with one another.

5. Results and Discussion

We now present the results of the analysis described above. Using the midplane densities of Section 4, we calculate according to the Poisson-Jeans equation the corresponding H_2 and HI surface densities, and from these we compute the chi-squared value, $(\Sigma - \hat{\Sigma})^2 / \Delta_{\Sigma}^2$, from the disagreement between these values and the measured values. This is done over a range of values for Σ_D and h_D . We thereby determine the regions of parameter space where the disagreement exceeds the 68% and 95% bounds, as will be displayed in the plots below. The scale height h_D is defined such that

$$\rho(Z=h_D) = \rho(Z=0) \text{sech}^2(1/2). \quad (61)$$

We begin by determining the bounds without including the contribution from magnetic fields and cosmic rays. The result is shown in Figure 4. The uncertainty H_2 is dominated by that of the dark molecular gas, while the uncertainty of HI is dominated by that of the WNM velocity dispersion (18%). We can see that although the H_2 parameters are consistent with dark disk surface densities of (for low scale height) up to $10 - 12 M_{\odot} \text{pc}^{-2}$, the HI parameters point toward lower

surface densities, and that the combined probabilities are lower than 9% for all models. These results make it apparent that the model without magnetic fields is inconsistent.

On the other hand, when we include the pressure contribution from the magnetic fields and from cosmic rays, we find that both the HI and H₂ parameters allow non-zero surface densities Σ_D , with an upper bound of $\Sigma_D \simeq 10 M_\odot \text{pc}^{-2}$ in both models, for low scale heights. Higher scale heights are consistent with even higher dark disk surface densities. The results are shown in Figure 5.

For comparison, we also include the corresponding results using the values of McKee et al. (2015). Using these values and including magnetic fields and cosmic ray contributions, the data favors a non-zero surface density for the dark disk of between 5 and 15 $M_\odot \text{pc}^{-2}$. Note that when neglecting magnetic field and cosmic rays pressures, only low dark disk surface densities seem consistent with the data.

Ionized Hydrogen Results and Issues

As was mentioned in Section 4.3, various authors have measured DM values for the HII component of the Milky Way in the range 20-30 $\text{cm}^{-3} \text{pc}$. Older models favored low scale height with midplane densities as high as 0.034cm^{-3} , while newer models favor large scale height models with midplane densities as low as 0.014cm^{-3} . However, using our model, the results of our Poisson-Jeans solver are consistent with only low scale heights. Following the models described in Section 4.4, we find scale heights for the HII of 0.9 kpc for the thermal scaling model and 1.0 kpc for the warm equipartition model, assuming $\Sigma_D = 0$. Incorporating a more massive dark disk makes these scale heights smaller. Possible reasons for this might be:

- 1) The magnetic field model must be modified to include a different value of α for HII. This could be in correspondence with the result of Beuermann et al. (1985), who found that Galactic magnetic fields contained two components, one with short scale height and one with larger scale height. These two components would likely be described by different α . We could then attribute the low scale height component to the molecular and atomic gas and the large scale height component to the ionized gas. We know of no such alternative in the warm equipartition model.
- 2) The isothermal assumption may not be valid for HII. In fact, as explained in Gaensler et al. (2008), the volume filling fraction of HII may also vary a lot with scale height. If this is the case, then it would be incorrect to treat the HII as an isothermal component as the degrees of freedom that the temperature describes (the gas clouds) vary with distance from the Galactic midplane.

Stability Issues and Kinematic Constraints

In Figure 7 we show the bound we obtained from the kinematics of A stars in the Solar region, accounting for nonequilibrium features of the population, namely a net displacement and vertical

velocity relative to the Galactic midplane. We also note that there will exist disk stability bounds. The true analysis is subtle, but a step toward the analysis is done by Shaviv (2016b) who develops the stability criterion for a heterogeneous Milky Way disk including a thin dark matter disk. We convert his bound to a bound in the $h_D - \Sigma_D$ plane and superimpose this bound on the gas parameter bound of the present work. We see that a disk with significant mass (Σ_D) and $h_D > 30$ pc is consistent with all current bounds.

In addition to stability issues, Hessman (2015) has argued that there exist other issues with using the vertical Jeans equation to constrain the dynamical mass in the MW disk. In particular, spiral structure must be taken into account when performing these analyses. Indeed, Shaviv (2016a) has pointed out that the effect of spiral arm crossing is to induce a ‘ringing’ in the dynamics of tracer stars. However, the present analysis assumes that the time scales for this ringing are much shorter in gas components so that the analysis is valid. Spiral arm crossing could also induce non-equilibrium features in the tracer population, such as discussed in Kramer & Randall (2016), but as in Kramer & Randall, including this effect would allow for more dark matter.

6. Conclusion

In this paper we have shown how to use measured midplane and surface densities of various galactic plane components to constrain or discover a dark disk. Although literature values of atomic hydrogen midplane densities are discordant, their mean value is consistent with the remaining gas parameters when magnetic and cosmic ray pressures are included. Using the global averages of literature values of gas parameters that we compiled, we find the data are consistent with dark disk surface densities as high as $10 M_\odot \text{pc}^{-2}$ for low scale height, and as low as zero. The gas parameters of McKee et al. (2015) seem to favor an even higher non-zero dark disk surface density. Current data are clearly inadequate to decide this definitively. Further measurements of visible and dark H_2 density and WNM density and dispersion, as well as further refinements of magnetic field and cosmic ray models for cold gas could allow placing more robust bounds on a dark disk.

We would like to thank Chris Flynn and Chris McKee for their comments and suggestions, and also for reviewing our results. We would also like to thank Johann Holmberg and Jo Bovy for useful discussions. Thanks also to Doug Finkbeiner, Jo Bovy, Alexander Tielens, Katia Ferrière, and Matt Walker for help on the ISM parameters. We would also like to thank our reviewer for their detailed review of our work. EDK was supported by NSF grants of LR and by Harvard FAS, Harvard Department of Physics, and Center for the Fundamental Laws of Nature. LR was supported by NSF grants PHY-0855591 and PHY-1216270. Calculations performed in MATLAB 2015a.

REFERENCES

- Bahcall, J. N. 1984a, *ApJ*, 287, 926
- . 1984b, *ApJ*, 276, 169
- . 1984c, *ApJ*, 276, 156
- Belfort, P., & Crovisier, J. 1984, *A&A*, 136, 368
- Beuermann, K., Kanbach, G., & Berkhuijsen, E. M. 1985, *A&A*, 153, 17
- Binney, J., & Merrifield, M. 1998, *Galactic Astronomy*
- Bohlin, R. C., Savage, B. D., & Drake, J. F. 1978, *ApJ*, 224, 132
- Boulares, A., & Cox, D. P. 1990, *ApJ*, 365, 544
- Bronfman, L., Cohen, R. S., Alvarez, H., May, J., & Thaddeus, P. 1988, *ApJ*, 324, 248
- Burton, W. B., & Gordon, M. A. 1978, *A&A*, 63, 7
- Clemens, D. P., Sanders, D. B., & Scoville, N. Z. 1988, *ApJ*, 327, 139
- Cordes, J. M., & Lazio, T. J. W. 2002, *ArXiv Astrophysics e-prints*, astro-ph/0207156
- Cordes, J. M., Weisberg, J. M., Frail, D. A., Spangler, S. R., & Ryan, M. 1991, *Nature*, 354, 121
- Dame, T. M., Hartmann, D., & Thaddeus, P. 2001, *ApJ*, 547, 792
- Dame, T. M., Ungerechts, H., Cohen, R. S., et al. 1987, *ApJ*, 322, 706
- Dickey, J. M., & Lockman, F. J. 1990, *ARA&A*, 28, 215
- Digel, S. W. 1991, PhD thesis, Harvard University, Cambridge, MA.
- Draine, B. T. 2011, *Physics of the Interstellar and Intergalactic Medium*
- Fan, J., Katz, A., Randall, L., & Reece, M. 2013, *Physics of the Dark Universe*, 2, 139
- Ferrière, K. M. 2001, *Reviews of Modern Physics*, 73, 1031
- Flynn, C., Holmberg, J., Portinari, L., Fuchs, B., & Jahreiß, H. 2006, *MNRAS*, 372, 1149
- Gaensler, B. M., Madsen, G. J., Chatterjee, S., & Mao, S. A. 2008, *PASA*, 25, 184
- Gillessen, S., Eisenhauer, F., Trippe, S., et al. 2009, *ApJ*, 692, 1075
- Grabelsky, D. A., Cohen, R. S., Bronfman, L., Thaddeus, P., & May, J. 1987, *ApJ*, 315, 122

- Heiles, C., & Crutcher, R. 2005, in *Lecture Notes in Physics*, Berlin Springer Verlag, Vol. 664, Cosmic Magnetic Fields, ed. R. Wielebinski & R. Beck, 137
- Heiles, C., Kulkarni, S., & Stark, A. A. 1981, *ApJ*, 247, L73
- Heiles, C., & Troland, T. H. 2003, *ApJ*, 586, 1067
- Hessman, F. V. 2015, *A&A*, 579, A123
- Heyer, M., & Dame, T. M. 2015, *ARA&A*, 53, 583
- Holmberg, J., & Flynn, C. 2000, *MNRAS*, 313, 209
- Kalberla, P. M. W. 2003, *ApJ*, 588, 805
- Kalberla, P. M. W., & Dedes, L. 2008, *A&A*, 487, 951
- Kalberla, P. M. W., Dedes, L., Kerp, J., & Haud, U. 2007, *A&A*, 469, 511
- Kalberla, P. M. W., & Kerp, J. 1998, *A&A*, 339, 745
- Kramer, E. D., & Randall, L. 2016, *ApJ*, 824, 116
- Kulkarni, S. R., & Heiles, C. 1987, in *Astrophysics and Space Science Library*, Vol. 134, *Interstellar Processes*, ed. D. J. Hollenbach & H. A. Thronson, Jr., 87–122
- Liszt, H. S. 1992, in *Astrophysics and Space Science Library*, Vol. 180, *The Center, Bulge, and Disk of the Milky Way*, ed. L. Blitz, 111–130
- Liszt, H. S., & Burton, W. B. 1983, in *Astrophysics and Space Science Library*, Vol. 100, *Kinematics, Dynamics and Structure of the Milky Way*, ed. W. L. H. Shuter, 135–142
- Luna, A., Bronfman, L., Carrasco, L., & May, J. 2006, *ApJ*, 641, 938
- McKee, C., Parravano, A., & Hollenbach, D. J. 2015, *ApJ*
- Nakanishi, H., & Sofue, Y. 2003, *Publ. Astron. Soc. Jap.*, 55, 191
- . 2006, *Publ. Astron. Soc. Jap.*, 58, 847
- Okumura, A., Kamae, T., & for the Fermi LAT Collaboration. 2009, *ArXiv e-prints*, arXiv:0912.3860
- Oort, J. H. 1932, *Bull. Astron. Inst. Netherlands*, 6, 249, 6, 249
- . 1960, *Bull. Astron. Inst. Netherlands*, 15, 45, 15, 45
- Parker, E. N. 1966, *ApJ*, 145, 811
- Pineda, J. L., Langer, W. D., Velusamy, T., & Goldsmith, P. F. 2013, *A&A*, 554, A103

- Planck Collaboration, Ade, P. A. R., Aghanim, N., et al. 2011, *A&A*, 536, A19
- Randall, L., & Reece, M. 2014, *Phys. Rev. Lett.*, 112, 161301
- Read, J. I. 2014, *Journal of Physics G Nuclear Physics*, 41, 063101
- Read, J. I., Lake, G., Agertz, O., & Debattista, V. P. 2008, *MNRAS*, 389, 1041
- Reynolds, R. J. 1985, *ApJ*, 294, 256
- Reynolds, R. J. 1991, in *IAU Symposium*, Vol. 144, *The Interstellar Disk-Halo Connection in Galaxies*, ed. H. Bloemen, 67–76
- Reynolds, R. J. 1992, in *American Institute of Physics Conference Series*, Vol. 278, *American Institute of Physics Conference Series*, 156–165
- Sanders, D. B., Solomon, P. M., & Scoville, N. Z. 1984, *ApJ*, 276, 182
- Schnitzeler, D. H. F. M. 2012, *MNRAS*, 427, 664
- Scoville, N. Z., & Sanders, D. B. 1987, in *Astrophysics and Space Science Library*, Vol. 134, *Interstellar Processes*, ed. D. J. Hollenbach & H. A. Thronson, Jr., 21–50
- Shaviv, N. J. 2016a, *ArXiv e-prints*, arXiv:1606.02595
- . 2016b, *ArXiv e-prints*, arXiv:1606.02851
- Taylor, J. H., & Cordes, J. M. 1993, *ApJ*, 411, 674
- Wouterloot, J. G. A., Brand, J., Burton, W. B., & Kwee, K. K. 1990, *A&A*, 230, 21

Fig. 2.— Molecular hydrogen midplane densities and surface densities determined by various authors between 1984 and 2006.

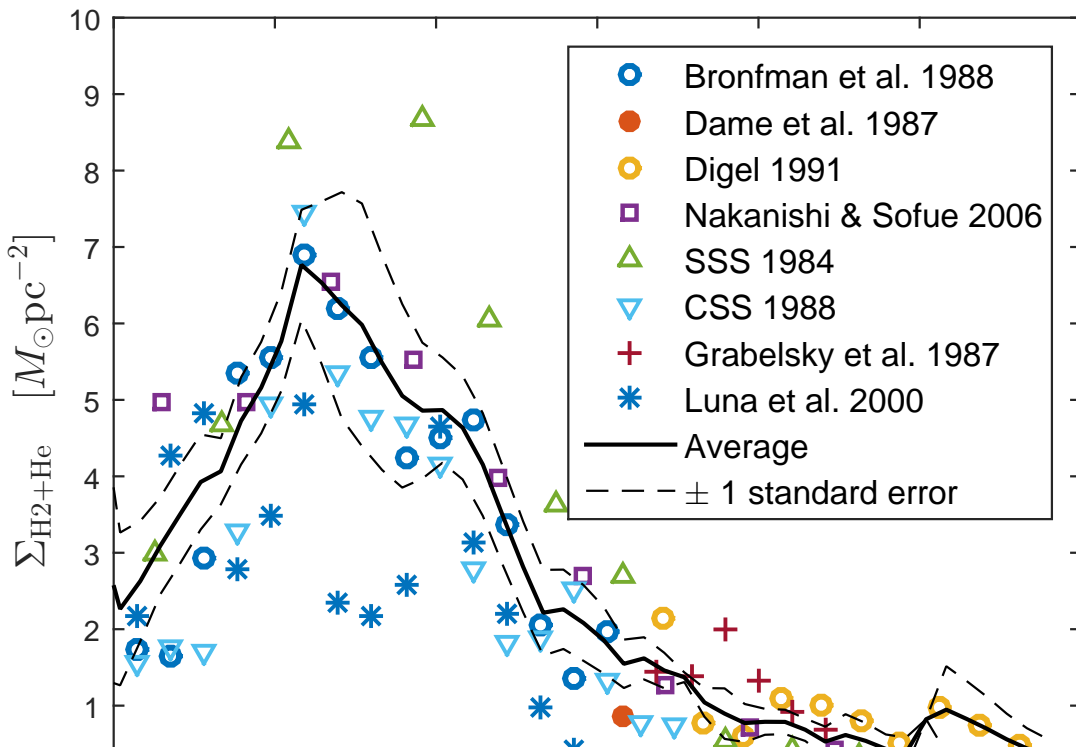
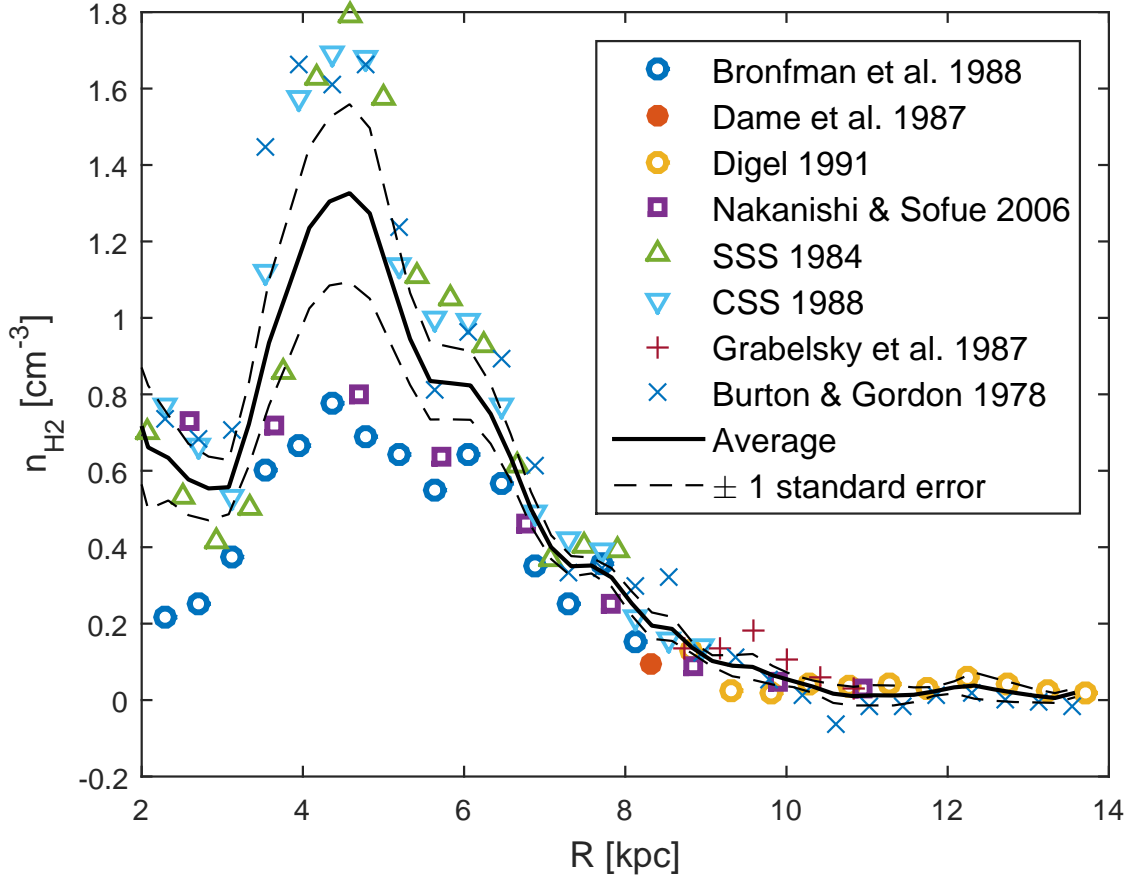


Fig. 3.— Atomic hydrogen midplane densities and surface densities determined by various authors between 1978 and 2008.

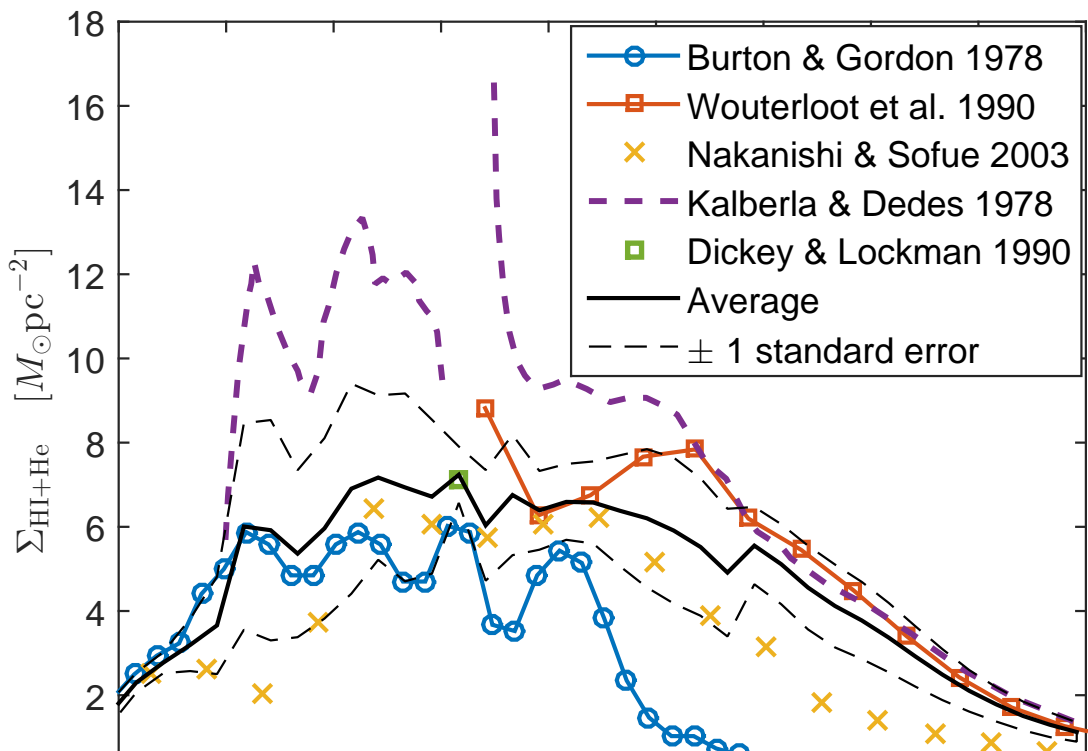
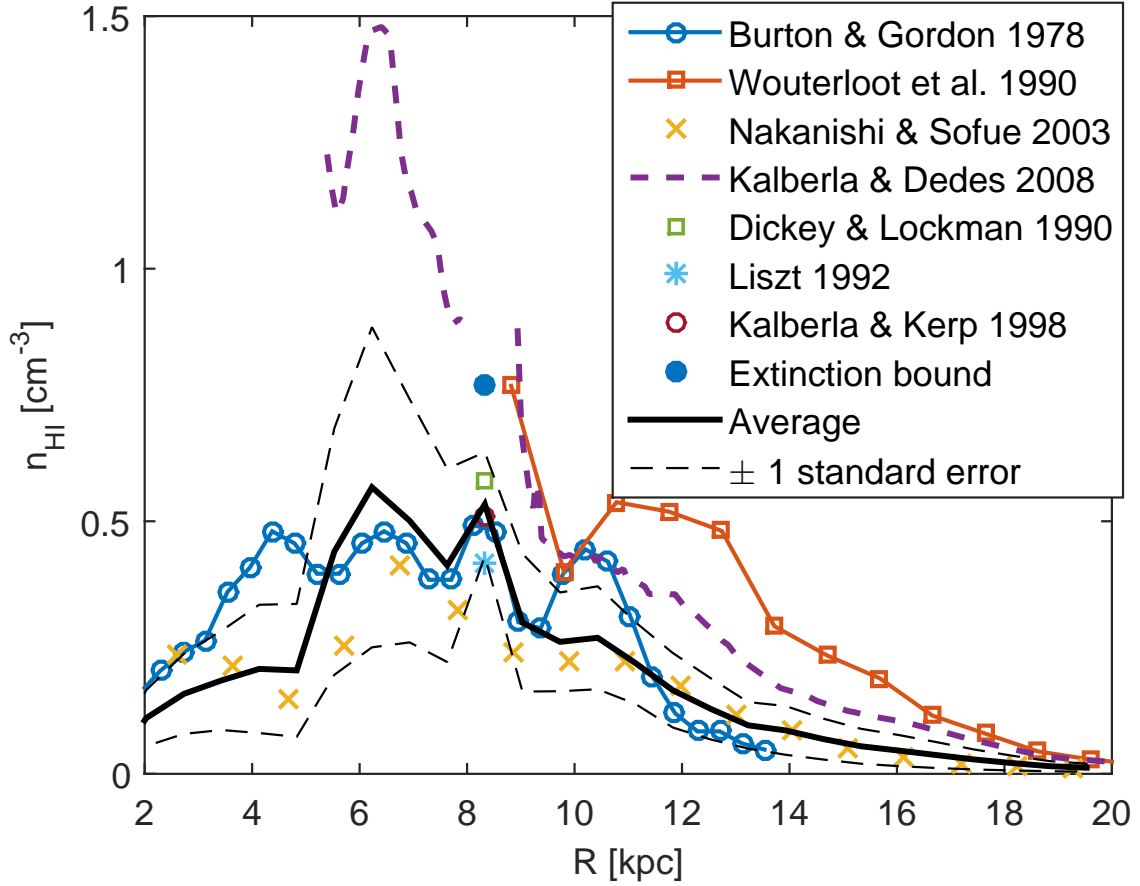


Fig. 4.— Confidence bounds on DDDM parameter space as a function of h_D , the dark disk $\text{sech}^2(z/2h_D)$ scale height, using averages and uncertainties from Sections 4.1 to 4.3. Solid lines represent 95% bounds and dashed lines represent 68% bounds.

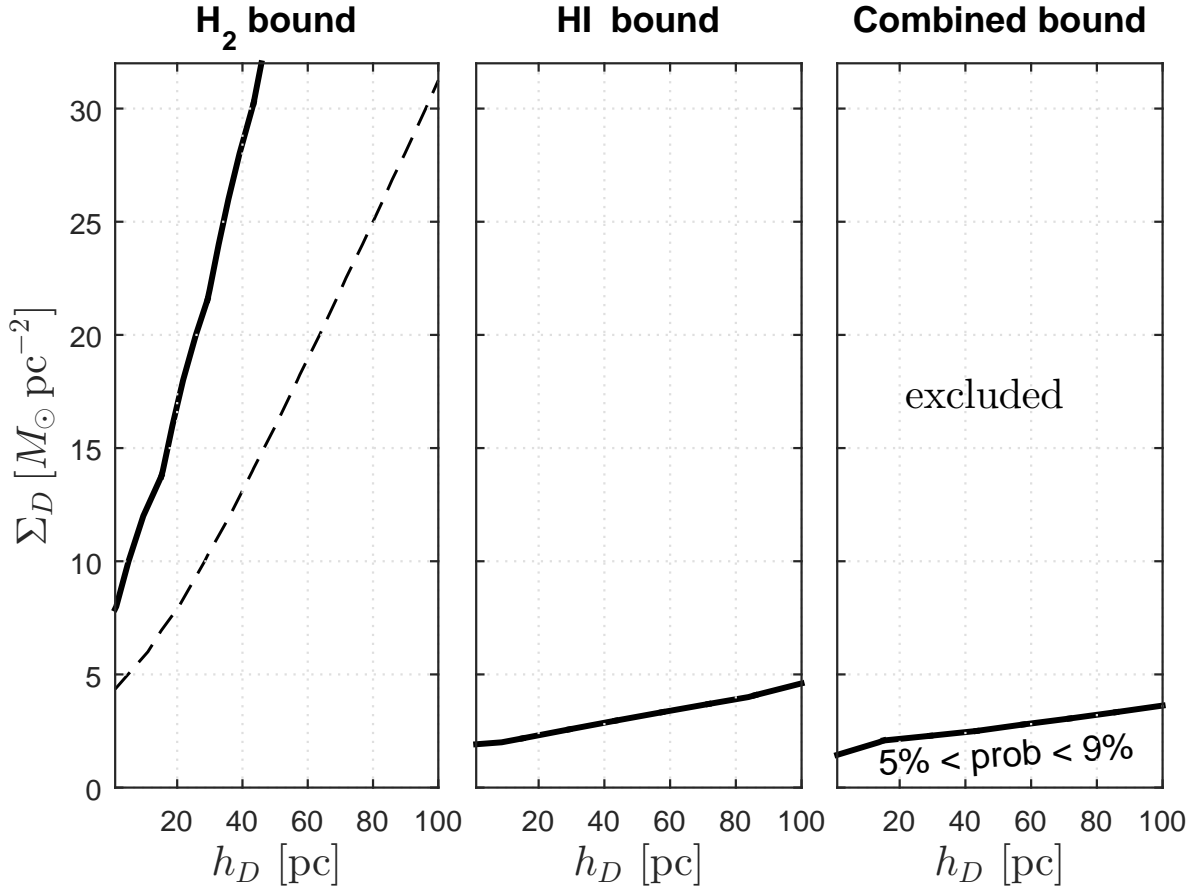


Fig. 5.— Bounds on DDDM parameter space as in Figure 4, but including contributions from magnetic fields and from cosmic rays. *Black*: computed assuming ‘thermal scaling model’. *Red*: computed assuming ‘warm equipartition model’.

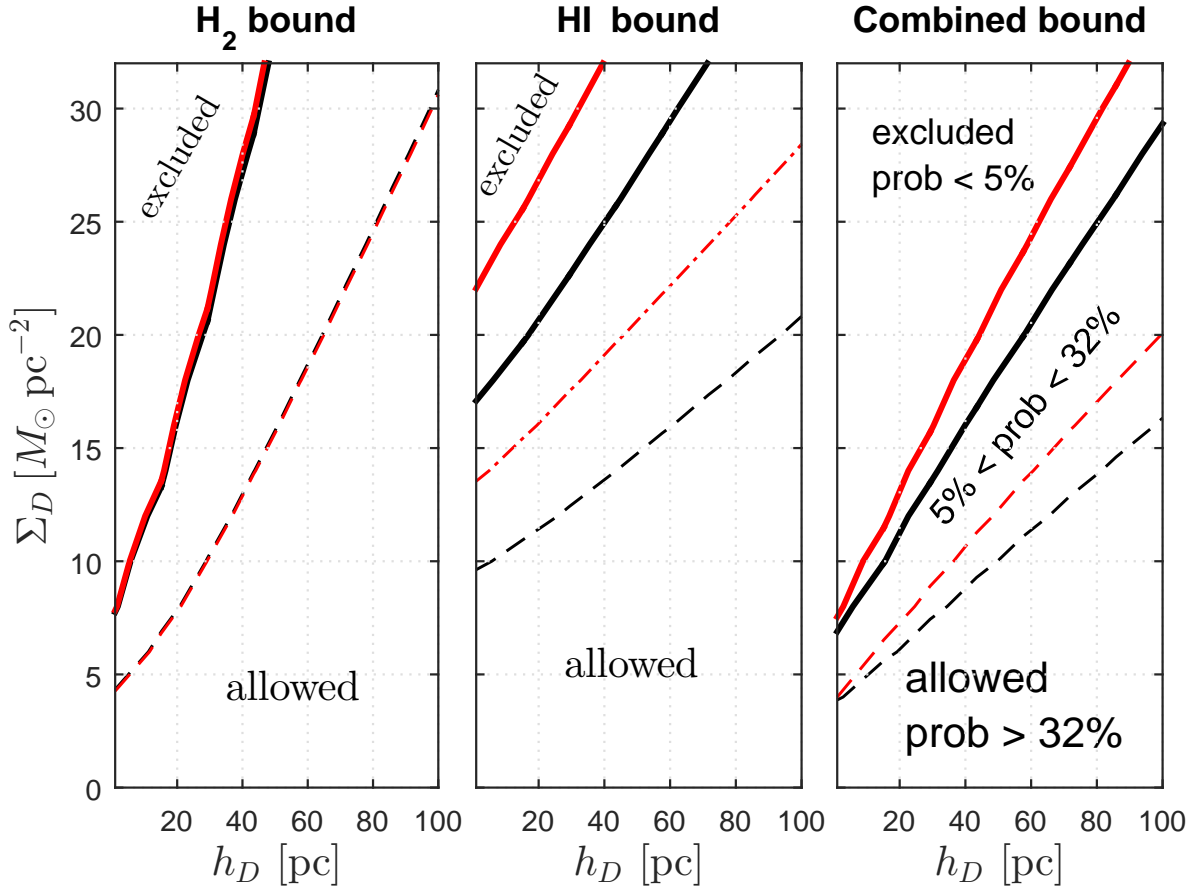


Fig. 6.— Confidence bounds as in Figure 4 but using the values of McKee et al. (2015). *Left*: Not including magnetic field and cosmic ray contributions. *Right*: including magnetic field and cosmic ray contributions as in Figure 5.

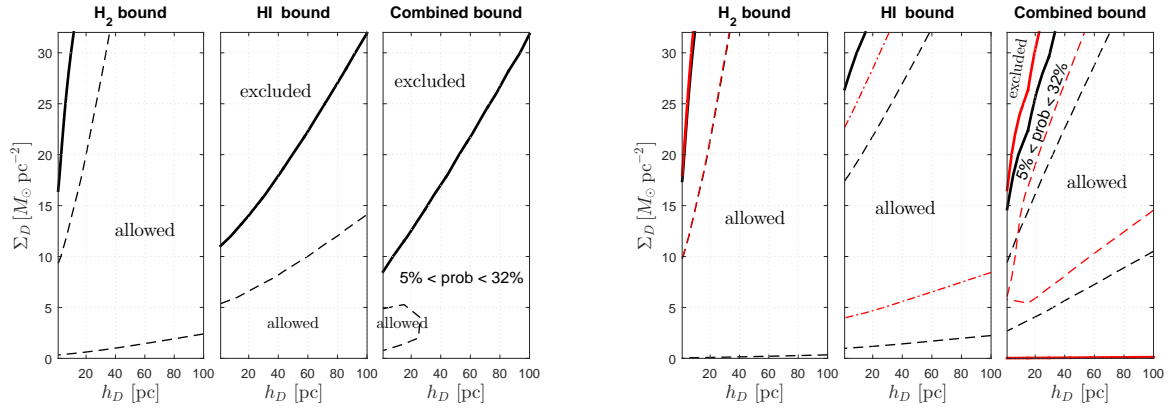


Fig. 7.— The red shaded region, delimited by the solid red line, denotes the parameters allowed by the stability bound of Shaviv (2016b). The blue shaded region, delimited by the solid blue line, denotes the parameters allowed by the kinematic bound of Kramer & Randall (2016). The grey shaded region, delimited by the solid black line, denotes the parameters allowed by the gas parameters as determined in the current paper. As in Figure 6, the dashed and solid black lines denote the 68% and 95% bounds obtained from the combined gas bound, including magnetic field and cosmic ray contributions, and using the parameters of McKee et al. (2015).

